RGNZ/MGPB

Rudarsko-geološko-naftni zbornik
(The Mining-Geology-Petroleum Engineering Bulletin)
UDC: 550.3
DOI: 10.17794/rgn.2025.2.4

Original scientific paper

# New Insight into the Structural Model in Southern Sumatra Indonesia using Gravity and Magnetic Data: Implications for Geothermal Resources

**Irfan Prasetyo[1]*; Wawan Gunawan Abdul Kadir[2]; Dadi Abdurrahman[3]; Darharta Dahrin[4]; Khalil Ibrahim[5]; Andri Kurniawan[6]**

[1]*Faculty of Mining and Petroleum Engineering, Bandung Institute of Technology, Indonesia. https://orcid.org/0009-0001-2372-8470*
[2]*Faculty of Mining and Petroleum Engineering, Bandung Institute of Technology, Indonesia.*
[3]*Faculty of Mining and Petroleum Engineering, Bandung Institute of Technology, Indonesia. https://orcid.org/0000-0001-7476-0174*
[4]*Faculty of Mining and Petroleum Engineering, Bandung Institute of Technology, Indonesia. Faculty of Industrial Technology, ITERA, Indonesia. https://orcid.org/0000-0003-1143-1060*
[5]*Faculty of Mining and Petroleum Engineering, Bandung Institute of Technology, Indonesia. https://orcid.org/0000-0002-7108-5457*
[6]*Faculty of Engineering, Lampung University, Indonesia. https://orcid.org/0009-0001-0761-7674*

## Abstract

The island of Sumatra was formed through complex tectonic processes that produce a variety of geological resources, including geothermal potential. Fault structures, particularly the Great Sumatran Fault (GSF), are associated with surface geothermal manifestations. The objective of this investigation is to conduct a thorough assessment of the geothermal potential in southern Sumatra by utilising a combination of magnetic and gravity data. The results show that the heat source in Sumatra is intrusive volcanic rocks with a density of 2.8 g/cm³ and a susceptibility value of 0.007, extending from west to south in a northwest-southeast pattern. These rocks are part of the Kikim Formation (Tpok) from the magma residue of Mount Bukit Besar, Bukit Lumut, and Bukit Balai, at a depth of more than 7 km. The reservoir layer in the center is likely caused by the Sumatra Fault fracture zone or sedimentary rocks, consisting of the Hulusimpang and Gumai formations, with a density of 2.6 g/cm³ and a susceptibility of 0.075 at a depth of 1000–1500 m. The heat flow ranges from 55.1 to 79 mW/m², and the geothermal gradient is between 21.1 and 31.6°C/km. Another finding is the high geothermal gradient observed beneath volcanic complexes, including the Bukit Barisan Mountains area. The northwest-southeast fault structure parallel to the GSF suggests that this fault controls the geothermal system in Sumatra, providing new insight into the fault control mechanism of the geothermal system. The integration of gravity and magnetic data reveals new relationships between tectonic structures in the GSF zone and previously unexplored geothermal potential.

**Keywords:**
gravity methods, magnetic methods, geothermal, Great Sumatran Fault

## 1. Introduction

Subduction of the Indo-Australian and Eurasian plates created the Sunda volcanic arc systems, of which Sumatra is a component. This process results in the formation of volcanoes along the arc. A significant geological feature in Sumatra is the Great Sumatran Fault, a dextral strike-slip fault zone known as the Great Sumatran Fault (GSF) (**Hamilton, 1979**; **Bellier and Sébrier, 1994**; **Sieh and Natawidjaja, 2000**; **Curray, 2005**; **Burton and Hall, 2014**; **Veloso et al., 2015; Natawidjaja et al., 2017**; **Widiantoro et al., 2024**). The GSF zone provides a complex geodynamic context and is one of the areas potentially most affected by significant tectonic activity (**Sukmono et al., 1996**; **Bellier et al., 1999**). The Great Sumatran Fault (GSF) is divided into 19 segments, including Semangko, Komering, Manna, and Ketaun in Southern Sumatra. Additionally, Patah Hill, Lumut Hill, and Balai Hill are part of the Bukit Barisan Mountains especially in Southern Sumatra. The hill is controlled by the SFZ structure, which is characterized by the presence of a caldera structure like the one on Lumut Hill. Generally, these hills are composed of young volcanic units consisting of andesite, breccia andesite, and basaltic andesite (**Nurseto et al., 2020**).

The Great Sumatran Fault (GSF) facilitates the upward flow of geothermal fluids through fractures and faults, making areas around GSF highly prospective for geothermal exploration due to permeable pathways created by tectonic activity. The island of Sumatra also has volcanic activity and geodynamic zones, which may indicate similar conditions for geothermal exploration. Further studies of near-surface magmatic activity and geodynamic conditions in Sumatra could help identify zones of high geothermal potential. Another indication

---

* Corresponding author: Irfan Prasetyo
*e-mail address: irfangeofisika@gmail.com*

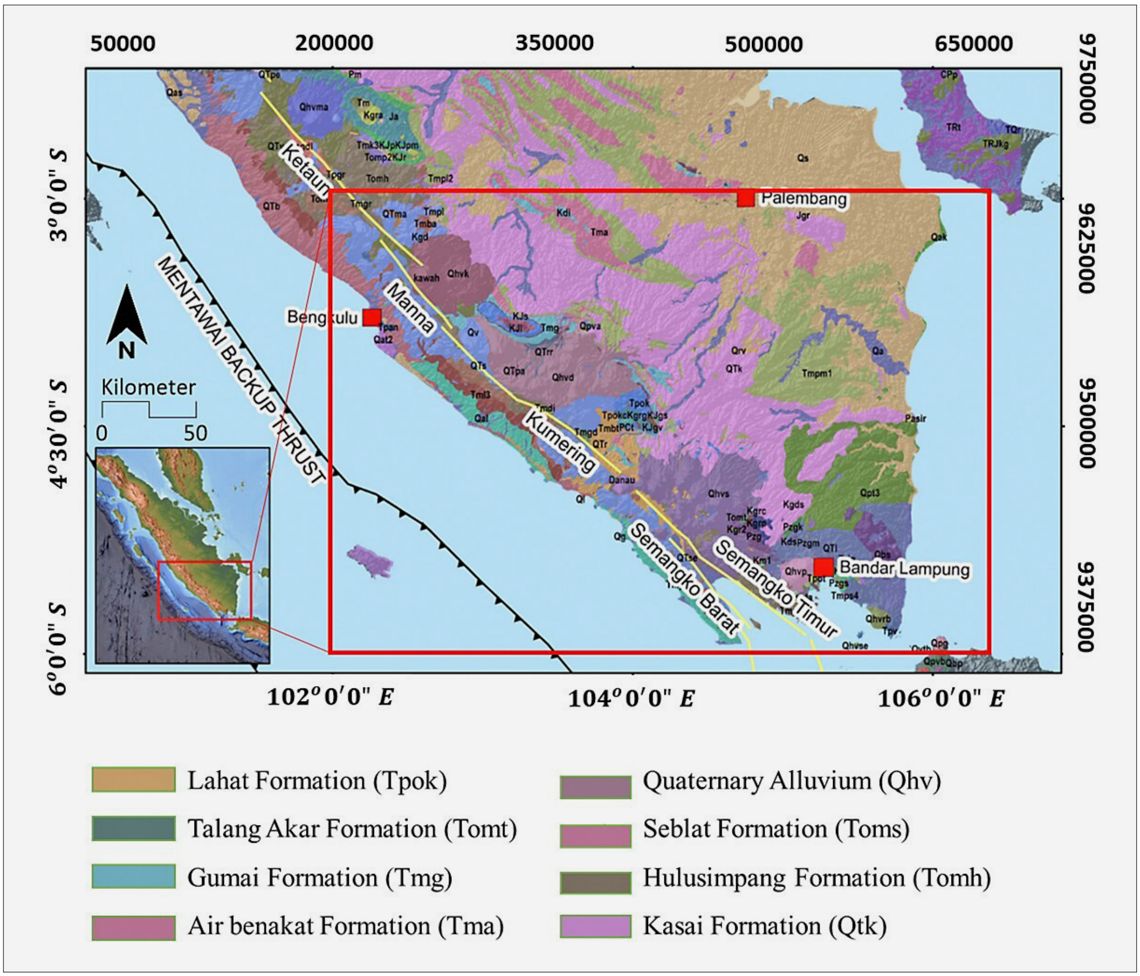

**Figure 1:** A geologic map showing the Great Sumatran Fault (GSF) in the southern part of Sumatra Island

of geothermal potential is the manifestation of hot water at the surface (**Hochstein et al., 1996**). This manifestation occurs due to the propagation of heat from below the surface and the existence of orientations such as fractures allowing the flow of geothermal fluid to rise to the surface, which is a characteristic feature of geothermal systems (**Siringoringo et al., 2024**).

This study focuses on the southern part of Sumatra, as shown in **Figure 1**. The study area crosses several fault segments, such as the Manna Fault Segment, the Kumering Fault Segment, and the Semangko Fault Segment. Several geophysical studies in the southern part of Sumatra Island show that there is volcanic activity in the Sumatra segment, which is characterized by a low velocity zone (**Liu et al., 2021**). **Hochstein et al. (1996)** relate volcanic activity to geothermal potential from various high-temperature systems and volcanic activity along the active Sumatran arc. Sumatra has at least half of its active volcanoes that are connected to volcanic geothermal reserves that hold magmatic gases and acidic fluids. This volcanic activity contributes to high geothermal gradients and the existence of geothermal systems. Due to the thinning of the continental crust and the presence of magma from the rising mantle, geochemical measurements from the southern island of Sumatra show high heat flow (**Siringoringo et al., 2024**).

Some previous researchers have focused on subsurface modelling and aspects of geological data for the Sumatra region. The integration of gravity and magnetic data has uncovered previously unexplored relationships between tectonic structures and geothermal anomalies. The combination of these two methods has been widely used in the identification of geothermal potential (**Moghaddam et al., 2016**; **Zaher et al., 2018**; **Zhang et al., 2020**; **Basantaray and Mandal, 2022**; **Gaber et al., 2024**; **Hilemichaeil et al., 2024**; **Kongpet and Kanjanapayont, 2024**). Gravity and magnetic methods of exploration of geothermal resources are quite effective because they can delineate geological structures in the form of faults (**Zhang et al., 2020**), which are very important in controlling the distribution of surface manifestations. Magnetic methods can estimate demagnetized rocks due to changes in temperature and acidity (**Kauffman and Keller, 1981**). To fill this knowledge gap, a geophysical technique makes use of the Curie point depth (CPD), where temperature approaches CPD of magnetite or loses magnetization (580°C) (**Abdel Zaher et al., 2018; Kongpet and Kanjanapayont, 2024**).

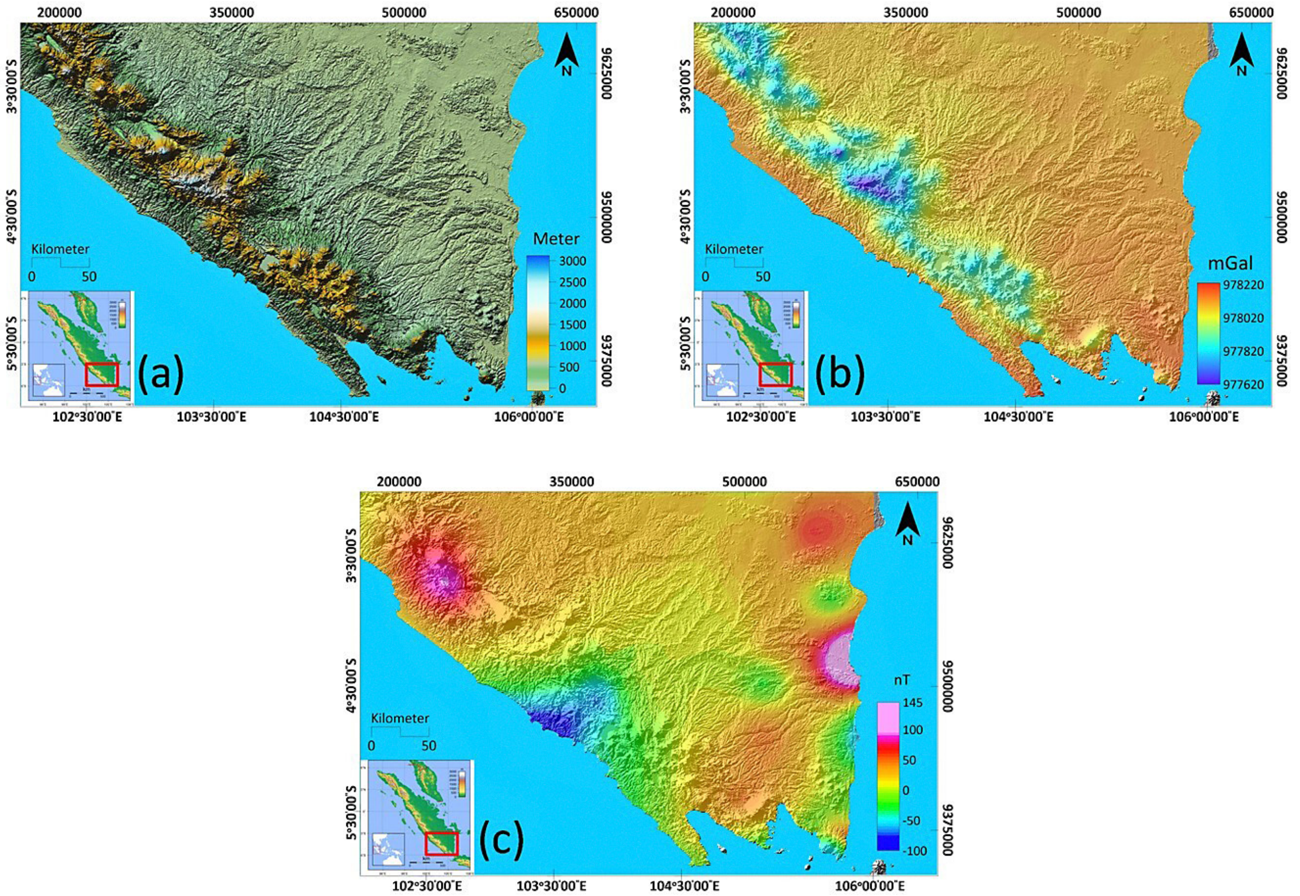

**Figure 2:** Research data: (a) a topographic map of the study area **Hirt et al. (2014)**; (b) gravity observation data from **Hirt et al. (2013)**; and (c) magnetic data from EMAG2v3 for the southern Sumatra region (**Meyer and Saltus, 2017**).

In this context, the objective of this investigation is to evaluate the gravity and magnetic response anomalies to estimate geothermal potential. Gravity research was conducted using high-resolution earth gravity information derived from the Global Gravity Model Plus (GGMplus) by **Hirt et al. (2013)**, Earth Residual Terrain Model (ERTM) 2160 by **Hirt et al. (2014)**, and Shuttle Radar Topography Mission version 2 Gravity (SRTM2gravity) by **Hirt et al. (2019)**. Meanwhile, magnetic research uses the Earth Magnetic Anomaly Grid 2-arc-minute resolution (EMAG2v3) by **Meyer and Saltus (2017)**. Furthermore, the data were combined to understand the subsurface geological structure, map lithological boundaries, and determine the depth and location of heat sources. In addition, the data were used for subsurface configuration and its association to thermal characteristics by identifying CPD to locate heat source. This analysis is supported by edge detection analysis using the Fast Sigmoid-Based Edge Detection (FSED) edge gradient technique (**Pham et al., 2023**). Edge detection techniques are capable of delineating fault structures (**Pham et al., 2023**; **Safani et al., 2023**; **Aprina et al., 2024; Pham and Prasad, 2024**). We performed quantitative interpretation to model the subsurface structure of a location using 2.5D joint forward modelling of gravity and magnetic data. This combination's results can help provide a conceptual model for the development of geothermal potential in southern Sumatra.

## 2. Material and methods

### *2.1. Data*

This research is located in southern Sumatra, within the geographical coordinates of 3°00'00" - 6°00'00" S and 102°00'00" - 106°30'00" E. Based on the UTM projection (datum 48S WGS84), the area is defined by UTM X coordinates ranging from 166,000 to 667,500 and UTM Y coordinates from 9,335,000 to 9,669,000, encompassing a total area of approximately 500 km by 400 km. **Figure 2** depicts the research area. The southern part of Sumatra Island is characterized by high topography known as the Bukit Barisan Mountains, which are situated in the west, and sediment is dominant in the east. The highest elevation on this island is 3,200 m (see **Figure 2a**). Research data collection in the form of satellite data from various sources includes GGMPlus gravity data (**Hirt et al., 2013**), total magnetic anomaly data from EMAG2v3 (**Meyer and Saltus, 2017**), topographic data from SRTM2610 (**Hirt et al., 2014**), and SRTM2gravity (**Hirt et al., 2919**).

This study used global gravity and magnetic data: GGMplus gravity acceleration and quasi-geoid (**Hirt et al., 2013**). Elevation data was collected from the GGMplus SRTM2160 gravity elevation reference model. The GGMplus gravity elevation reference model uses residual SRTM2gravity data to correct the free air anomaly (FAA) data. Additionally, magnetic data were obtained from EMAG2v3, which is the latest version of EMAG2 with a resolution of 2 arc minutes with an upward continuation of 4 km (**Meyer and Saltus, 2017**).

## 2.2. *Processing gravity data*

### 2.2.1. Average density estimation

This study uses the Parasnis method to estimate the average density (**Rao and Satyanarayana, 1973**), with calculations showing a consistent value of 2.3 g/cc for the study area. **Figure 3** illustrates the calculated average density value. Using this value as a variable, the Complete Bouguer Anomaly (CBA) for southern Sumatra can be determined.

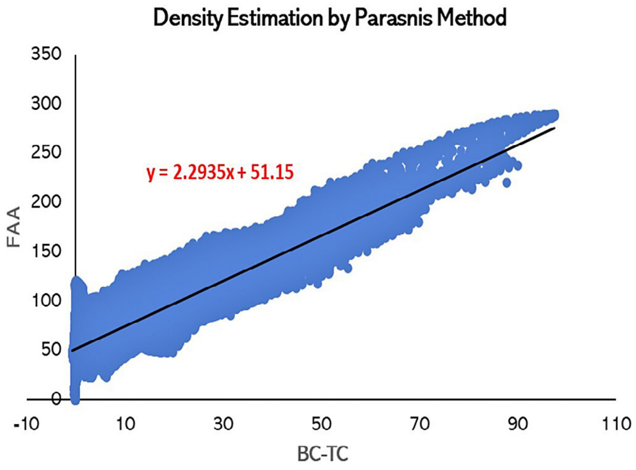

**Figure 3:** Average density estimation results of the Parasnis method

### 2.2.2. Analysis of the Power Spectrum

Spectrum analysis is performed to estimate the window width and depth of gravity anomalies. Additionally, spectrum analysis can be used to compare the spectrum responses of various filtering methods. Spectrum analysis is conducted by Fourier transforming predefined tracks. The Fourier transformation of gravity anomalies observed in the horizontal plane is provided (**Blakely, 1996**). The window width estimation is conducted to determine the window width that will be used to separate regional and residual data. To obtain an optimal window width estimation, the amplitude spectrum resulting from the above Fourier transformation (**Equation 1**) is logarithmized, yielding a straight-line equation. The component $k$ becomes directly proportional to the amplitude spectrum.

$$Ln\ P = \left(z_0 - z'\right)|k| \tag{1}$$

From the equation above, linear regression is used to obtain the boundary between the first order (regional) and the second order (residual), with the value of ($k$) at this boundary taken as the determinant of the window width. The relationship between wavelength ($\lambda$) and ($k$) is derived from the equation (**Blakely, 1996**) where ($n$) is the window width.

$$k = \frac{2\pi}{\lambda}; \lambda = n \cdot \Delta x \tag{2}$$

### 2.2.3. Separation of the gravity anomaly

The moving average method (**Robinson, 1988**) is used in this study with a 21x21 grid point window and 2 km grid spacing to separate the Bouguer anomaly's parts, such as surface noise, residual, and regional anomalies. This technique produces more accurate anomaly maps and facilitates geophysical interpretation, which is essential for identifying deep geological features and removing noise effects. **Equation 3** mathematically displays the moving average equation for the 1-D case.

$$\Delta g_r(a) = \frac{\Delta g(a-n) + \ldots + \Delta g(a) + \ldots + \Delta g(a+n)}{N} \tag{3}$$

Applying a moving average to a two-dimensional map, the value of $\Delta g_R$ at a point can be calculated by averaging all the values of $\Delta g_R$ in a square box, with the center point being the point from which the value of $\Delta g_R$ will be calculated. **Equation 4** provides an example of applying a moving average in a 5x5 window on two-dimensional data.

$$\Delta g_R = \frac{1}{25} \cdot \left[\left(\Delta g_{B1}\right) + \left(\Delta g_{B2}\right) + \left(\Delta g_{B3}\right) + \ldots\ldots + \left(\Delta g_{B25}\right)\right] \tag{4}$$

### 2.2.4. Edge detection filter

Techniques of edge detection are utilised to identify the boundary of the anomaly cause. Fast Sigmoid Edge Detection, also referred to as FSED, is one of the techniques. FSED is an edge detection filter that gives the maximum amplitude to the anomaly source's edge. According to **Oksum et al. (2021)** and **Pham et al. (2023)**. Anomalies from both deep and shallow geological origins can be balanced simultaneously by this filter. **Equation 5** illustrates this technique mathematically.

$$FSED = \frac{R-1}{1+|R|} \tag{5}$$

$$R = \frac{\dfrac{\partial HG}{\partial z}}{\sqrt{\left(\dfrac{\partial HG}{\partial x}\right)^2 + \left(\dfrac{\partial HG}{\partial y}\right)^2}} \tag{6}$$

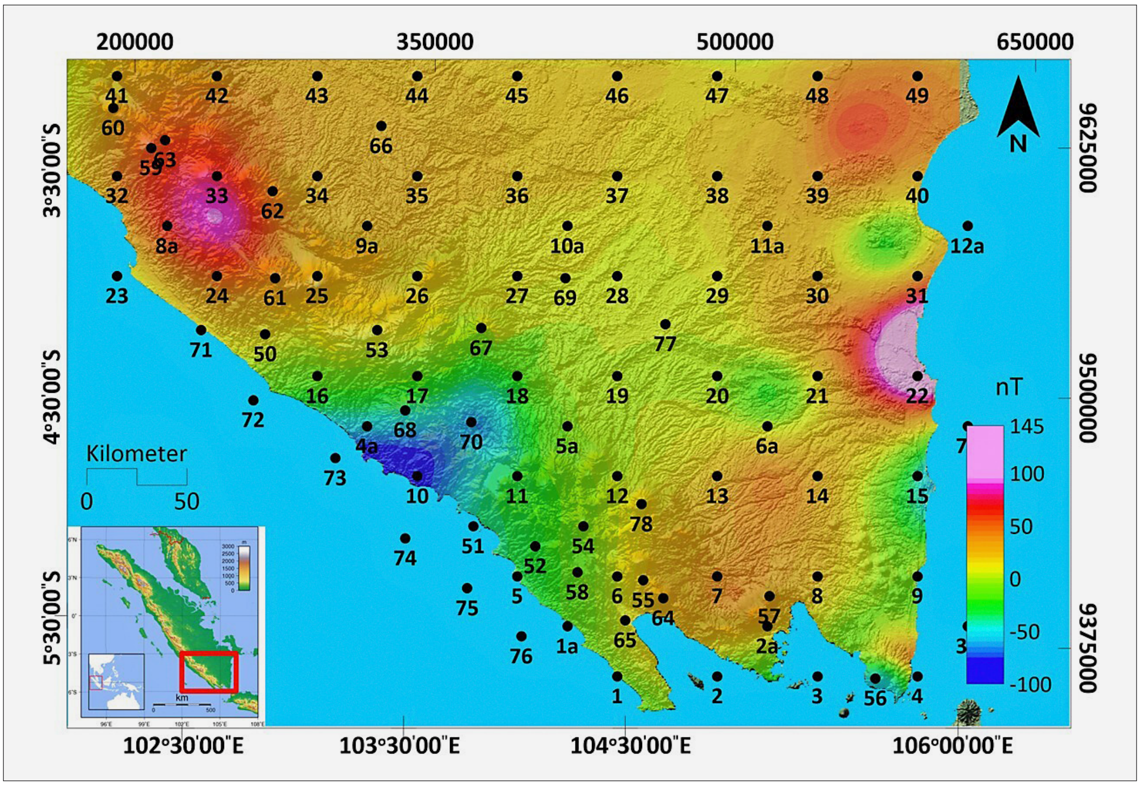

**Figure 4:** Distribution map of CPD estimation points with a 100 km x 100 km window width

## *2.3. Processing magnetic data*

### 2.3.1. Reduce to pole from magnetic data

Reduce to the pole (RTP) transformation is a standard method for eliminating dipolar effects (**Cooper and Cowan, 2005**). According to the International Geomagnetic Reference Field (IGRF), RTP uses an inclination of -8.1° and a declination of -0.01°. **Finlay et al. (2010)** adjusted the magnetic anomaly to conditions of 90° inclination and 0° declination.

### 2.3.2. Curie Point Depth

Curie Point Depth (CPD) is the depth at which the Curie temperature is reached by minerals in the Earth's crust, marking the point where the geological materials that make up the lithosphere transition from the ferromagnetic phase to the paramagnetic phase (**Okubo et al., 1985**). The magnetization of rocks is influenced by their composition, specifically the quantity of magnetic minerals they contain, and by the temperature. When calculating the thickness of the Earth's magnetized crust, it becomes evident that two issues related to vertical compositional changes lead to rocks losing their ferromagnetic properties (**Abdel Zaher et al., 2018; Núñez Demarco et al., 2021**; **Kongpet and Kanjanapayont, 2024**). The magnetic properties of rocks are primarily influenced by ferromagnetic minerals, as the majority of minerals are paramagnetic or diamagnetic and exhibit extremely low magnetic susceptibility (**Núñez Demarco et al., 2021**).

**Okubo et al. (1985)** devised spectral analysis techniques that conducted CPD calculations from magnetic data in the study area. **Spector and Grant (1970)** invented the fundamental 2D spectral analysis technique for estimating the peak depth of a magnetic rectangular prism (Zt) from the slope of a log power spectrum**. Bhattacharyya and Leu (1975, 1977)** advanced this technique to determine the depth of the center of mass of a magnetic source object (Z0). Later, **Okubo et al. (1985**) developed a method to estimate the bottom depth of a magnetic source (*Zb*). For a two-dimensional body with a random, uncorrelated magnetization distribution, the power density spectrum, *P*(*k*), of the total magnetic field is expressed in terms of the top depth and thickness of the magnetic body (**Blakely, 1995**) and can be simplified as shown in **Equation 7**.

$$P(k) = Ae^{-2|k|Z_t}\left(1-e^{-|k|(Z_b-Z_t)}\right)^2 \tag{7}$$

where *k* is the magnetic field wavenumber and *A* is a constant. The depths of the magnetic source to the top and bottom are denoted by *Zt* and *Zb*, respectively.

For magnetic bodies that are thicker, the right side of **Equation 7** is reduced to **Equation 8.**

$$P(k) = Ae^{-2|k|Z_t} \tag{8}$$

This equation is illustrated in **Equation 9** for wavelengths that are less than twice the thickness of the layer.

$$\ln\left[P(k)^{\frac{1}{2}}\right] = A - |k| Z_t \tag{9}$$

The radially averaged power spectrum's slope for the higher wave number part is used to estimate the magnetic source's top depth (*Zt*).

**Equation 10**, which was adapted from **Okubo et al. (1985)** and **Tanaka et al. (1999)**, is used to estimate the depth to centroid depth (*Z0*) of deeper magnetic sources by dividing the slope of the lower wavenumber of the radially averaged power spectrum by the wavenumber.

$$\ln\frac{[P(k)^{1/2}]}{k} = B - |k| Z_o \tag{10}$$

where B is a constant. **Okubo et al. (1985)** have determined that the magnetic source's lower bound (**Equation 11**) can be calculated as:

$$Z_b = 2Z_0 - Z_t \tag{11}$$

$Z_b$ is presumed to represent the Curie point depth, which is the depth at which ferromagnetic minerals transition to paramagnetic minerals at a temperature of 580°C for magnetite.

The temperature gradient *($dT/d_z$ )* within the study area was estimated utilizing the equation formulated by **Tanaka et al. (1999)**, as presented in **Equation 12**.

$$\frac{dT}{d_z} = \frac{580^0 C}{Zb} \tag{12}$$

**Equation 13** defines the mathematical correlation between the temperature gradient and the heat flow (q).

$$q = kc\left(\frac{dT}{dz}\right) \tag{13}$$

where $k_c$ represents heat conductivity, the average thermal conductivity values for the oceans crust and continental crust are 2.0 W/m°C and 2.5 W/m°C, respectively.

The CPD mapping technique utilizes wavelength magnetic anomalies related to substantial magnetic sources within the Earth's crust, extending to depths of several tens of kilometres. To improve the accuracy and spatial continuity of the CPD map, the CPD is calculated within a square magnetic data window with a 50% overlap. The distribution of CPD calculation points in the study data is illustrated in **Figure 4**.

## 3. Results

### 3.1. Gravity anomaly

The radially averaged power spectrum, or RAPS, depicted in **Figure 5** demonstrates the calculated average depth for each of the segments. We performed RAPS analysis on the CBA data by performing a Fourier transform to generate amplitude (*A*) and wave number (*k*). We then present the results in a graph to estimate depth. The spectral analysis yielded anomaly depth values and wave number (*k*) cut-off values, revealing a steep gradient indicating a regional anomaly depth of 19.8 km, residual anomaly depth of 3.4 km, and noise at depth of 1.4 km.

The complete Bouguer anomaly contains information about anomalies at regional and local depths (see **Figure 6**). Separation of the local and regional components is an important step in gravity studies in the Bouguer anomaly, especially in geothermal exploration. **Figure 6** displays the gravity anomalies in the area, ranging from 15 to 111 mGal. The north and center primarily exhibit low anomalies (15–47 mGal) due to the deeper bedrock and thick layers of sedimentary rocks. The high anomalies (79–111 mGal) in the west and south are likely due to the exposure of bedrock at the surface, which has a higher density than the surrounding rocks (see **Figure 6a**).

In this study, the moving average technique is employed to enhance the accuracy of the anomaly map, allowing for better identification of geological features at greater depths and reducing the impact of near-surface noise. We eliminate regional anomalies to acquire residual anomalies that originate from the target source. The regional anomalies show values between 20 - 86

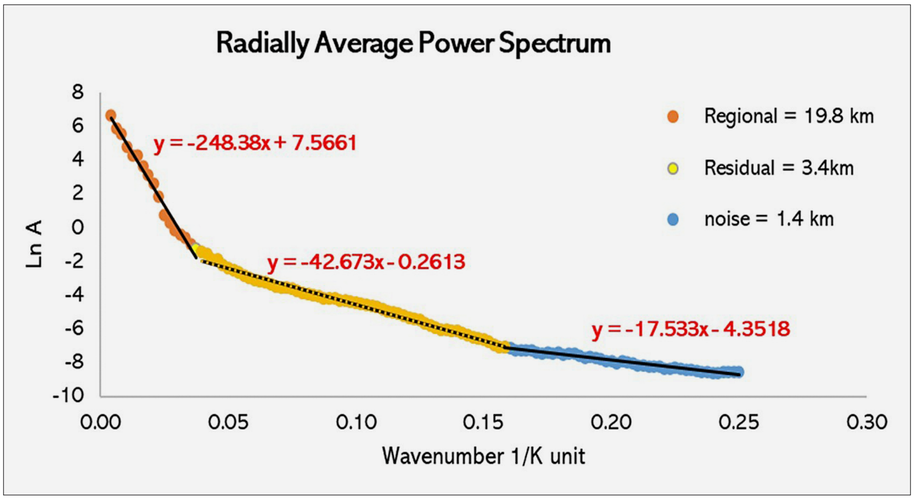

**Figure 5:** Radial average power spectrum curve graph of southern Sumatra Island CBA data

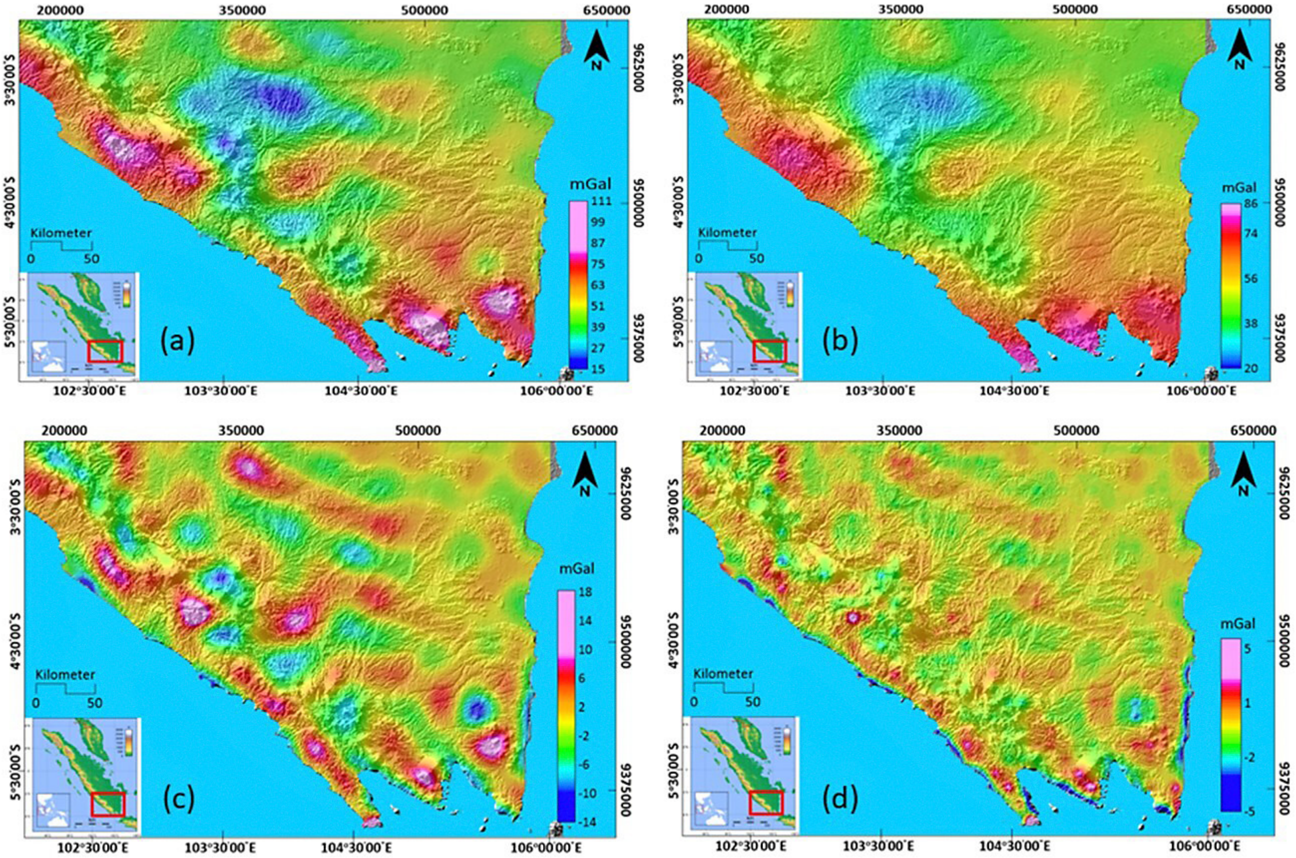

**Figure 6:** (a) Complete Bouguer anomaly map; (b) regional gravity anomaly map, (c). gravity residual anomaly map and (d) gravity anomaly noise map.

mGal, with high anomalies dominant in the west and south, following a northwest-southeast pattern (see **Figure 6b**). The residual anomalies, ranging from -14 - 18 mGal, are influenced by anomalous objects that are relatively shallower and near the surface, illustrating the geological structure of the study area (see **Figure 6c**). The noise sources are also shown in **Figure 6d**.

## *3.2. Edge detection*

In the application of FSED edge detection, calculations are performed based on **Equation 5**. The positive amplitude peaks from the FSED are used to identify the boundaries of geological structures. Fault structures are characterized by abrupt changes and steep gradients, while lithological boundaries produce smoother anomalies with gradual gradient changes; a combination of methods such as FSED analysis and correlation with geological maps can ensure accurate interpretation (**Pham dkk., 2023; Aprina dkk., 2024**). **Figure 7a** shows the interpretation results of the boundary of lineament obtained from the FSED technique. The lineament pattern formed has a northwest – southeast (NW-SE) direction, in accordance with the direction of the GSF structure the distribution of sedimentary basins. In **Figure 7b**, the lineament of the fault structure is marked with a red line, which is dominant along the west, which is the Bukit Barisan mountain complex. The yellow line shows the interpretation of lithological boundaries or rock formations with lineament patterns that follow the direction of the fault structure in the study area (see **Figure 7b**).

## *3.3. Magnetic anomaly*

The application of RTP to the magnetic anomaly data produced a map showing anomalous values within the range of -200 nT to 200 nT. High anomalies ranging from 80 nT to 200 nT are predominantly seen in the western region, following a northwest to southeast direction (see **Figure 8**). These are in line with the residual anomalies from gravity data, which suggests that there may be complex geological structures there, like faults, folds, magma intrusions, or zones with a lot of minerals. In the central region of the study area, the low anomalies ranging from -200 nT to -80 nT may be attributed to non-ferromagnetic rocks such as sandstone, clay, or volcanic rocks, which lack magnetic minerals.

## *3.4. Curie Point Depth*

For depth estimation, the area of interest should be at least three to four times the depth of the magnetic source (**Saada et al., 2021**), which represents the ideal window size for determining the target depth. According to the gravity data's RAPS analysis, the boundary of the re-

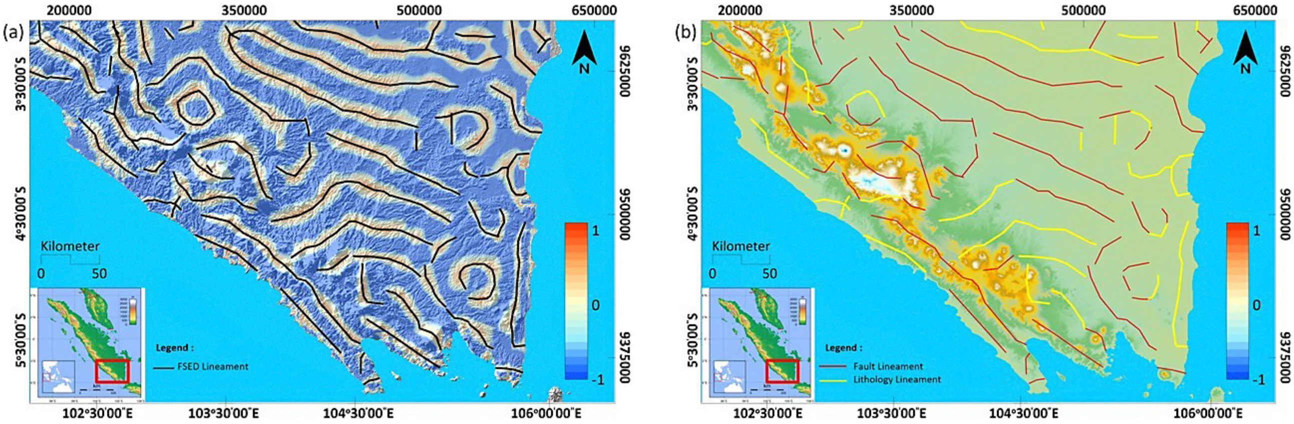

**Figure 7:** Interpretation of the geologic structure on southern Sumatra Island: (a) interpretation map of margin boundary with FSED and (b) Interpretation map of lithologic boundary and fault lineament.

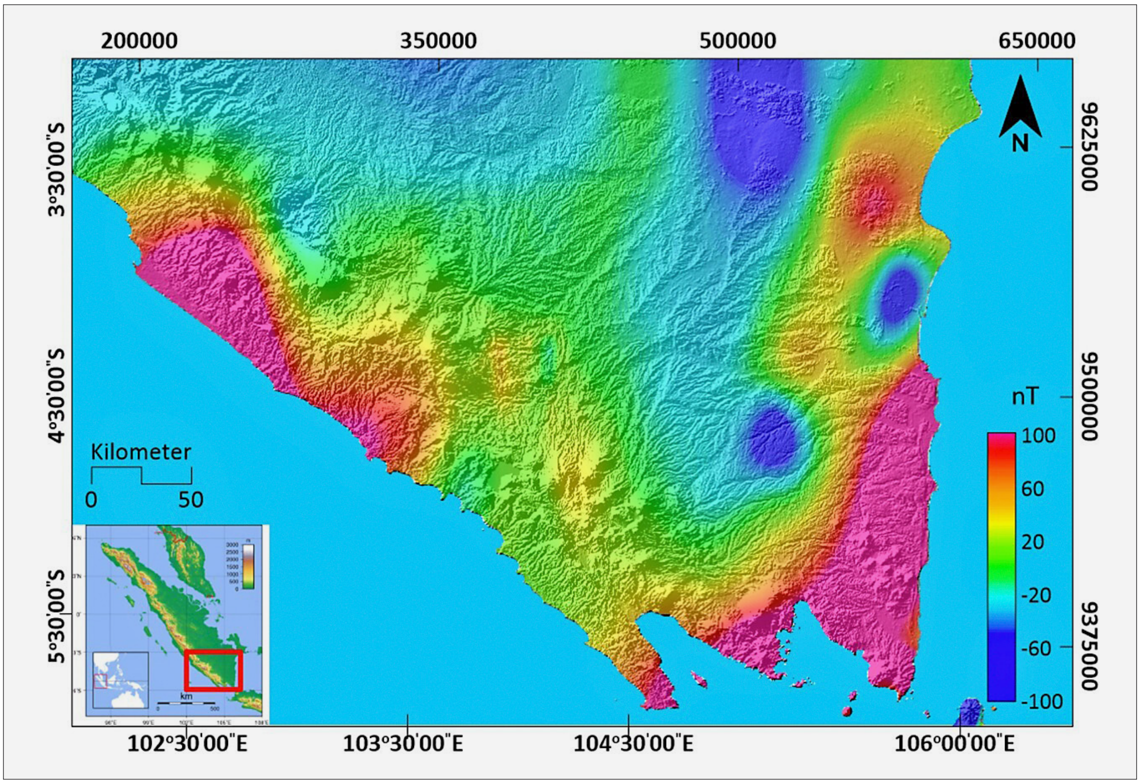

**Figure 8:** Magnetic anomaly map after reduce to pole

gional anomalies is 19.8 km. Therefore, the window width used for the CPD calculation is 100 km x 100 km, with 78 points scattered as shown in **Figure 4** to obtain the depth of the upper boundary ($Z_t$) and centroid boundry ($Z_0$). From **Figure 9**, the depth $Z_0$ is 13.45 km, calculated from the (regional) low-frequency gradient of 169.03, divided by 4π, following **Spector and Grant (1970)** methodology. **Figure 9** shows a depth $Z_t$ of 4.92 km from the (residual) low-frequency gradient of 61.875 rad, divided by 4π.

Follow the steps outlined in **Figure 9**. **Table 1** displays the estimated depth of the CPD for each block, along with the geothermal gradient and heat flow values for each segment. The heat flow value distribution is illustrated in **Figure 10**.

The depth of CPD ranges 18.4 km to 26.3 km. Heatflow and CPD plots show an inverse relationship in the study area. This means that as surface heatflow increases, CPD values are likely to decrease, and vice versa. The relationship may indicate a link between the surface heatflow distribution and the subsurface structure (see **Figure 10**). The thermal gradient values range 21.1 - 31.6°C/km. We detected the lowest thermal gradient of 21.1°C/km in the eastern part. The existence of a substantial sedimentation zone in the eastern region, where the topography tends to be lower, likely influences this,

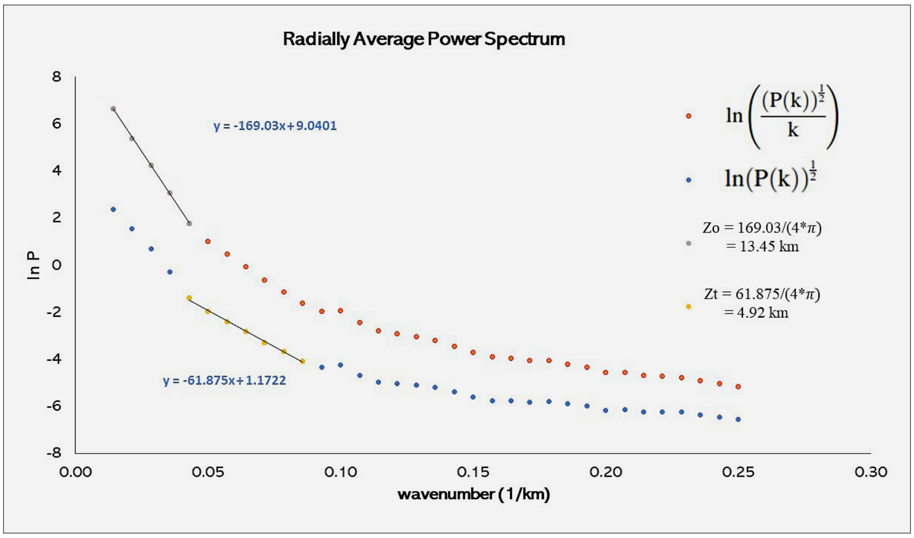

**Figure 9:** Radially averaged power spectrum CPD of block 1

unlike the western region where the volcanic complex of Bukit Barisan dominates. We have observed high thermal gradients beneath volcanic complexes, including the Bukit Barisan Mountains, reaching values of up to 31.6°C/km. This finding suggests a close relationship between the presence of volcanic complexes and significant geothermal activity. Seismic tomography modeled by **Liu et al. (2021)** shows volcanic activity below 30 km in the southern Sumatra region. This activity is defined by the presence of numerous geothermal manifestations on the surface, such as hot springs and fumaroles. These manifestations suggest an ongoing, active magmatic process under the volcano. This magmatic process contributes to heating subsurface water, which subsequently ascends to the surface as hot springs.

The observed heatflow values range from 55.1 - 79 mW/m², giving an idea of the heatflow distribution conditions in the area (see **Figure 10**). This range of values indicates a significant variation in the distribution of heat in the subsurface. The average heatflow of 67.8 mW/m² indicates a consistent geothermal anomaly in the region. However, of particular interest is the high maximum heatflow value of 79 mW/m². **Figure 10** is often associated with active volcanic regions, where volcanic activity drives higher than average heatflow. This result aligns with the findings of **Siringoringo et al. (2024)**, who propose that the heat flow observed from boreholes in the Sumatra region is due to both the thinning of the continental crust and the ascent of magma to the surface. This finding strengthens the hypothesis that the area has the geological characteristics of an active volcanic region due to subduction on the island of Sumatra.

In addition, the cause of the inverse relationship between heat flow and CPD values can vary and is highly dependent on site-specific geologic conditions. For example, geothermal activity in the subsurface can cause a significant increase in heat flow, where high heat from the geothermal source can cause a decrease in CPD values due to the increased temperature at a given depth. The occurrence is the result of a rise in temperature, which can modify the physical and thermal characteristics of rocks beneath the surface, therefore impacting the entire distribution of temperature. Conversely, high CPD values can indicate the presence of cold, dense rock layers in the subsurface that inhibit heat flow. These rock layers have low thermal conductivity. This suggests that the measured heat flow is consistent even when there are potential heat sources located below. In other words, high CPD values indicate that the cold rock can effectively absorb and trap heat, which in turn affects the relationship between heat flow and CPD values (**Kongpet and Kanjanapayont, 2024**).

## 4. Discussions

### *4.1. Geothermal potenty in Southern Sumatra*

The geothermal potential was evaluated by analysing gravity and magnetic data. The geothermal potential is depicted through various analyses that have been conducted. One indication of a geothermal system is the appearance of geothermal manifestations on the surface, such as hot water, fumaroles, steamy ground, warm water, and mud pools. These manifestations usually appear in weak zones or fault systems. On the residual gravity anomaly map, these weak zones or faults are situated at the boundary between regions of high and low anomalies (see **Figure 11**). Edge detection in gravity data facilitates geological interpretation, as lineament in gravity fields often reveal subsurface contacts, faults, and other tectonic features. Positive values above 0 in the FSED filter signify edge boundaries, interpreted as faults and lithologic boundaries (**Pham et al., 2023; Aprina et al., 2024; Pham and Prasad, 2024**).

A low gravity anomaly typically suggests the presence of a substantial sedimentary deposit. Typically, these zones have low densities compared to the surrounding rocks. In addition, the low contrast anomaly is

**Table 1:** Calculation result of Curie Point Depth (CPD) estimation

| Block | Zo | Zt | Zb | dT/dz | Heat flow |
|---|---|---|---|---|---|
| 1a | 13.5 | 4.9 | 22.0 | 26.4 | 66.0 |
| 2a | 13.7 | 5.8 | 21.6 | 26.9 | 67.2 |
| 4a | 12.9 | 3.9 | 21.9 | 26.5 | 66.2 |
| 5a | 11.2 | 3.5 | 18.8 | 30.8 | 77.1 |
| 6a | 13.8 | 3.1 | 24.6 | 23.6 | 59.0 |
| 7a | 14.1 | 5.1 | 23.2 | 25.0 | 62.6 |
| 8a | 12.6 | 4.8 | 20.3 | 28.5 | 71.3 |
| 9a | 12.1 | 5.1 | 19.0 | 30.5 | 76.2 |
| 10a | 13.4 | 7.9 | 18.8 | 30.8 | 77.1 |
| 11a | 14.1 | 4.8 | 23.5 | 24.7 | 61.7 |
| 12a | 14.1 | 4.3 | 24.0 | 24.1 | 60.4 |
| 1 | 12.0 | 3.5 | 20.4 | 28.4 | 71.0 |
| 2 | 13.6 | 4.7 | 22.6 | 25.7 | 64.2 |
| 3 | 12.8 | 5.0 | 20.6 | 28.2 | 70.4 |
| 4 | 12.0 | 0.6 | 23.3 | 24.9 | 62.2 |
| 5 | 14.3 | 7.7 | 20.8 | 27.9 | 69.7 |
| 6 | 11.4 | 4.4 | 18.5 | 31.3 | 78.3 |
| 7 | 11.8 | 3.7 | 19.9 | 29.1 | 72.7 |
| 8 | 12.5 | 4.1 | 20.8 | 27.8 | 69.6 |
| 9 | 13.7 | 4.0 | 23.3 | 24.9 | 62.2 |
| 10 | 14.7 | 8.3 | 21.2 | 27.4 | 68.5 |
| 11 | 11.1 | 3.4 | 18.8 | 30.8 | 77.1 |
| 12 | 12.4 | 3.1 | 21.7 | 26.7 | 66.8 |
| 13 | 12.9 | 3.6 | 22.1 | 26.2 | 65.6 |
| 14 | 13.8 | 3.3 | 24.3 | 23.8 | 59.6 |
| 15 | 13.9 | 4.2 | 23.6 | 24.5 | 61.4 |
| 16 | 12.3 | 3.4 | 21.1 | 27.4 | 68.6 |
| 17 | 11.0 | 2.9 | 19.2 | 30.3 | 75.7 |
| 18 | 10.6 | 1.5 | 19.8 | 29.3 | 73.3 |
| 19 | 11.8 | 4.3 | 19.3 | 30.1 | 75.1 |
| 20 | 14.9 | 5.3 | 24.5 | 23.7 | 59.3 |
| 21 | 14.4 | 4.4 | 24.4 | 23.7 | 59.3 |
| 22 | 14.7 | 4.9 | 24.4 | 23.8 | 59.4 |
| 23 | 13.2 | 4.9 | 21.5 | 27.0 | 67.4 |
| 24 | 12.4 | 4.3 | 20.6 | 28.2 | 70.5 |
| 25 | 12.3 | 5.3 | 19.3 | 30.1 | 75.2 |
| 26 | 11.2 | 2.9 | 19.6 | 29.6 | 74.0 |
| 27 | 11.3 | 2.6 | 20.0 | 29.0 | 72.5 |
| 28 | 11.4 | 2.4 | 20.3 | 28.5 | 71.3 |
| 29 | 13.3 | 3.1 | 23.5 | 24.7 | 61.7 |
| 30 | 13.0 | 3.1 | 22.9 | 25.3 | 63.4 |
| 31 | 14.2 | 3.7 | 24.8 | 23.4 | 58.4 |
| 32 | 13.4 | 4.4 | 22.4 | 25.9 | 64.8 |
| 33 | 12.4 | 5.1 | 19.7 | 29.4 | 73.6 |
| 34 | 12.6 | 5.2 | 19.9 | 29.1 | 72.8 |
| 35 | 12.8 | 3.5 | 22.1 | 26.2 | 65.6 |
| 36 | 13.5 | 4.0 | 23.0 | 25.2 | 63.0 |
| 37 | 14.0 | 4.0 | 24.0 | 24.1 | 60.3 |
| 38 | 14.1 | 3.4 | 24.8 | 23.4 | 58.5 |
| 39 | 14.1 | 3.0 | 25.2 | 23.0 | 57.5 |
| 40 | 14.0 | 3.1 | 24.9 | 23.3 | 58.2 |
| 41 | 11.4 | 3.9 | 19.0 | 30.5 | 76.2 |
| 42 | 11.6 | 2.2 | 21.1 | 27.5 | 68.7 |
| 43 | 13.7 | 4.3 | 23.1 | 25.1 | 62.7 |
| 44 | 12.8 | 4.7 | 20.9 | 27.8 | 69.5 |
| 45 | 13.3 | 3.7 | 22.9 | 25.3 | 63.3 |
| 46 | 13.0 | 2.4 | 23.5 | 24.6 | 61.6 |
| 47 | 13.9 | 2.5 | 25.3 | 22.9 | 57.3 |
| 48 | 14.1 | 3.0 | 25.2 | 23.0 | 57.4 |
| 49 | 14.4 | 2.5 | 26.3 | 22.1 | 55.1 |
| 50 | 13.3 | 5.3 | 21.3 | 27.2 | 68.0 |
| 51 | 12.9 | 4.0 | 21.7 | 26.7 | 66.7 |
| 52 | 11.9 | 3.2 | 20.7 | 28.0 | 70.0 |
| 53 | 12.0 | 4.8 | 19.3 | 30.1 | 75.2 |
| 54 | 11.7 | 4.5 | 18.8 | 30.8 | 77.0 |
| 55 | 13.0 | 5.0 | 21.0 | 27.6 | 69.0 |
| 56 | 10.7 | 1.4 | 20.0 | 29.1 | 72.7 |
| 57 | 11.0 | 3.0 | 19.0 | 30.6 | 76.5 |
| 58 | 11.4 | 3.0 | 19.9 | 29.2 | 73.0 |
| 59 | 11.5 | 2.9 | 20.1 | 28.8 | 72.0 |
| 60 | 12.2 | 4.6 | 19.9 | 29.2 | 72.9 |
| 61 | 13.1 | 4.7 | 21.5 | 27.0 | 67.4 |
| 62 | 11.9 | 3.9 | 19.8 | 29.3 | 73.2 |
| 63 | 11.2 | 3.0 | 19.4 | 29.9 | 74.7 |
| 64 | 11.9 | 3.3 | 20.5 | 28.4 | 70.9 |
| 65 | 10.7 | 2.1 | 19.2 | 30.2 | 75.5 |
| 66 | 11.3 | 3.3 | 19.3 | 30.1 | 75.2 |
| 67 | 11.3 | 2.9 | 19.7 | 29.4 | 73.5 |
| 68 | 11.9 | 3.4 | 20.4 | 28.5 | 71.2 |
| 69 | 10.8 | 2.5 | 19.0 | 30.6 | 76.5 |
| 70 | 10.6 | 2.9 | 18.4 | 31.6 | 79.0 |
| 71 | 14.5 | 4.1 | 24.8 | 23.4 | 58.4 |
| 72 | 14.4 | 4.6 | 24.2 | 24.0 | 59.9 |
| 73 | 13.1 | 4.2 | 21.9 | 26.4 | 66.1 |
| 74 | 14.3 | 5.3 | 23.4 | 24.8 | 62.0 |
| 75 | 13.8 | 3.2 | 24.4 | 23.8 | 59.5 |
| 76 | 13.7 | 2.4 | 24.9 | 23.3 | 58.2 |
| 77 | 12.4 | 4.8 | 20.0 | 29.0 | 72.4 |
| 78 | 11.8 | 2.8 | 20.7 | 28.0 | 70.0 |

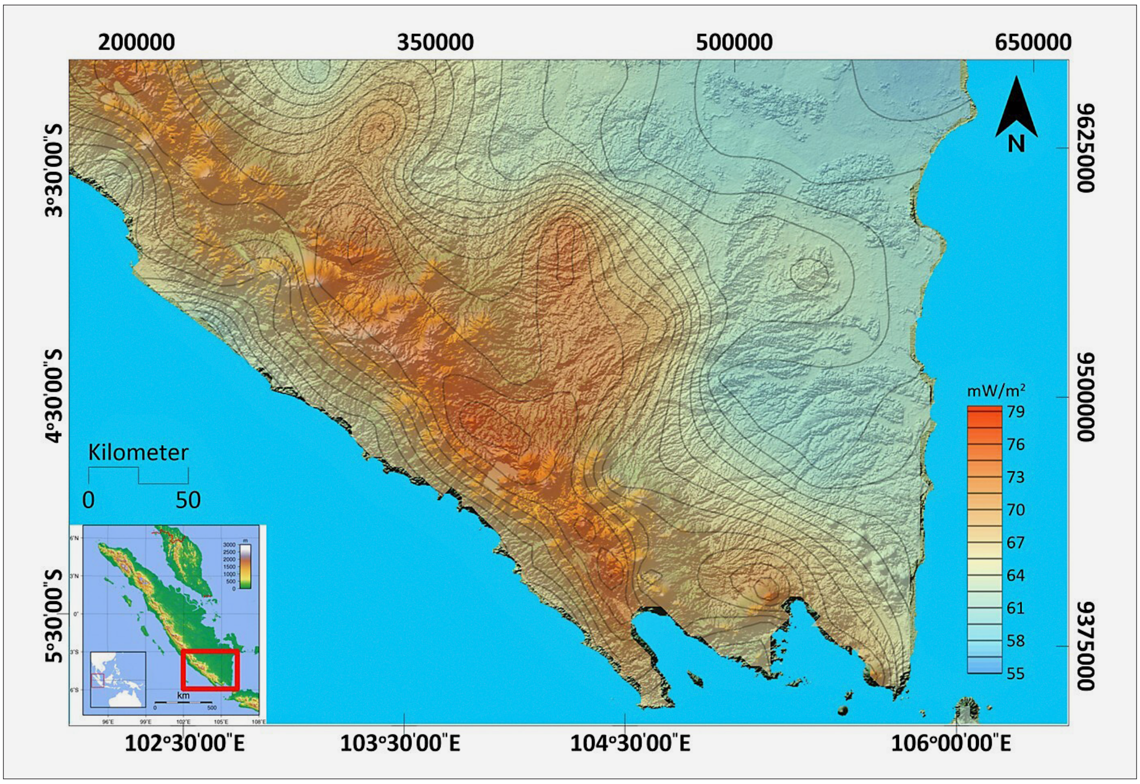

**Figure 10:** Heat flow RTP map of CPD (curie temperature 580°C, λ=2.5 W/m²)

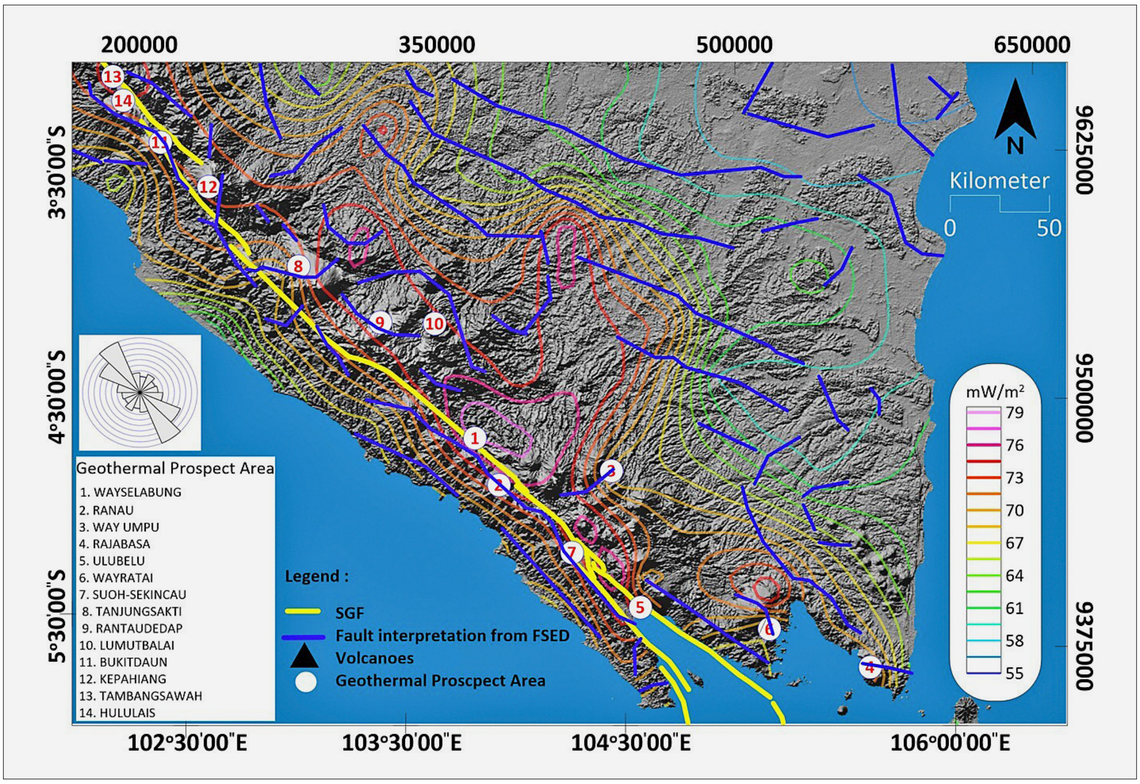

**Figure 11:** Geothermal prospect zone interpretation

situated in the southern part of the GSF. We suspect the effect of the Sumatran Fault in lowering the value of the gravity anomaly. The interpretation of the suspected GSF segment, derived from the FSED analysis, reveals that the fault structure trend in the southern Sumatra region is oriented northwest-southeast (NW-SE) (**Burton**

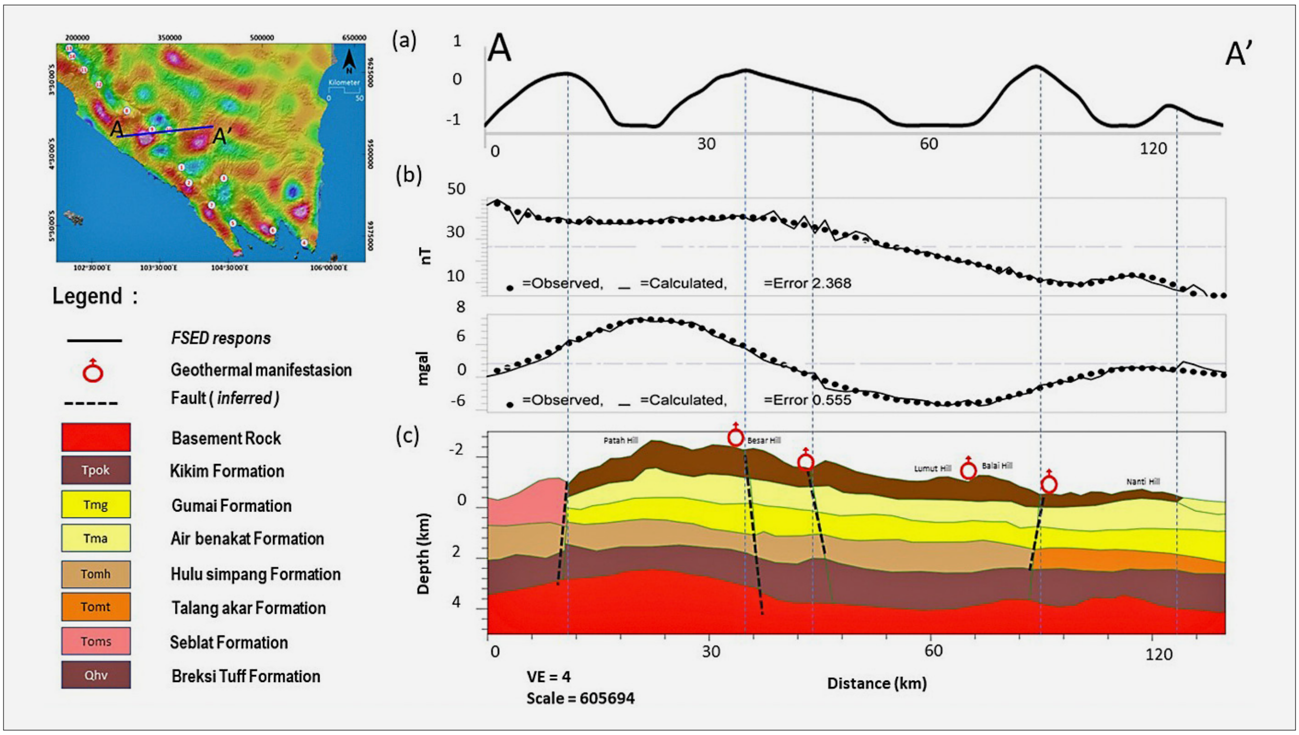

**Figure 12:** Cross-section A-A' of gravity and magnetic data modelling: (a) FSED response delineating the geological structure, (b) residual gravity and magnetic response and (c) 2.5D gravity model of the geothermal prospect area.

**and Hall, 2014; Natawidjaja et al., 2017; Alif et al., 2020**). Rose diagrams were used to analyse their orientation. The rose diagram is a visual tool for illustrating the orientation and frequency of fault structures, which can be created in QGIS by importing geospatial data and calculating the direction of the faults. Once the direction data is obtained, users can use the Processing Toolbox to generate a rose diagram that shows the distribution patterns of the faults. The use of rose diagrams helps to see the trend of the GSF in the southern part. This structural trend is also not continuous, so it is interpreted that there are several large segments in southern Sumatra. The identified faults include (1) the Manna segment, (2) the Kumering segment, and the West and East Semagko segments (see **Figure 11**).

## *4.2 Geological model interpretation*

In this research, 2.5D modelling is performed with the forward modelling method using residual gravity anomaly data, magnetic data that has been RTP, and supporting data such as regional geology, surface appearance, and rock density from measuring rock samples in volcanic areas in southern Sumatra by the **Geological Resources Center (PSDG) (2004)**. The modelling of 2.5D gravity data relied on these data for support. We constructed a subsurface model cross-section that crosses the mountain range and intersects four northwest-southeast trending faults. This model is also supported and accommodated by the lithological conditions in **Figure 1**. **Figures 12, 13,** and **14** are the results of joint forward modelling of gravity and magnetic data. The interpretation of the subsurface model indeed benefits from a clear connection between parts (a) and (b). **Figures 12a, 13a,** and **14a** show the response profiles filtered by the FSED filter, which enhances the structural boundaries that are visualized in the cross-section models in **Figures 12c, 13c, and 14c. Figures 12b** and **12c** display the gravity, magnetic responses, and the subsurface model in sections A-A', which span approximately 100 km and reach a depth of approximately 7,000 meters. This model interprets seven lithologies.

Tuff breccia (Qhv) with a density of 2.1 - 2.2 gr/cm$^3$ and a rock susceptibility value of 0.001– 0.002 sus is at the surface with a depth varying from 0 m to 1,000 m. This rock was formed by volcanic eruptions. Seblat (Toms) Formation, with a density of 2.2–2.3 gr/cm$^3$ and a rock susceptibility value of -0.008–0.0014 sus, is located on the surface at the western end of lines D–D' at a depth of 0–800 m. The Air Benakat formation, with a density of 2.4–2.5 gr/cm$^3$ and a rock susceptibility value of 0.003 to 0.0031 sus, is located at a depth of 1,000 - 1,500 m. Gumai Formation, with a density of 2.5–2.61 gr/cm$^3$ and a rock susceptibility of -0.0026-0.119 sus, is located at a depth of 1,500–2,500 m. Hulusimpang Formation (Tomh) with a density of 2.5–2.6 gr/cm$^3$ and a rock susceptibility of 0.0075-0.202 sus, located at a depth of 2,000–3,000 m. At a depth of 2,000–3,000 meters, the Talangakar Formation is situated with a rock susceptibility value of 0.065–0.003 sus and a density of 2.5–2.7 gr/cm$^3$. The Kikim Formation, which is situated at a depth of 3,000–5,000 m and is in close proximity to

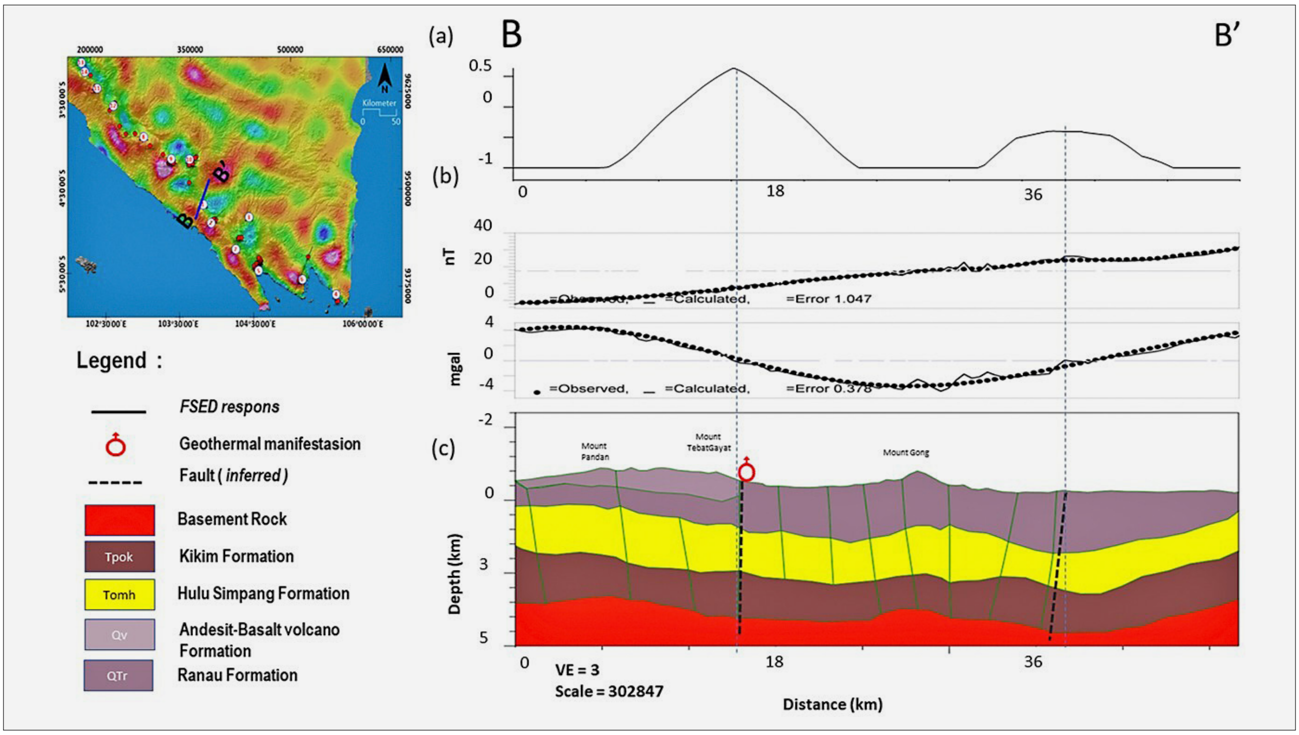

**Figure 13:** Cross-section B-B' of gravity and magnetic data modelling: (a) FSED response delineating the geological structure, (b) residual gravity and magnetic response and (c) 2.5D gravity model of the geothermal prospect area.

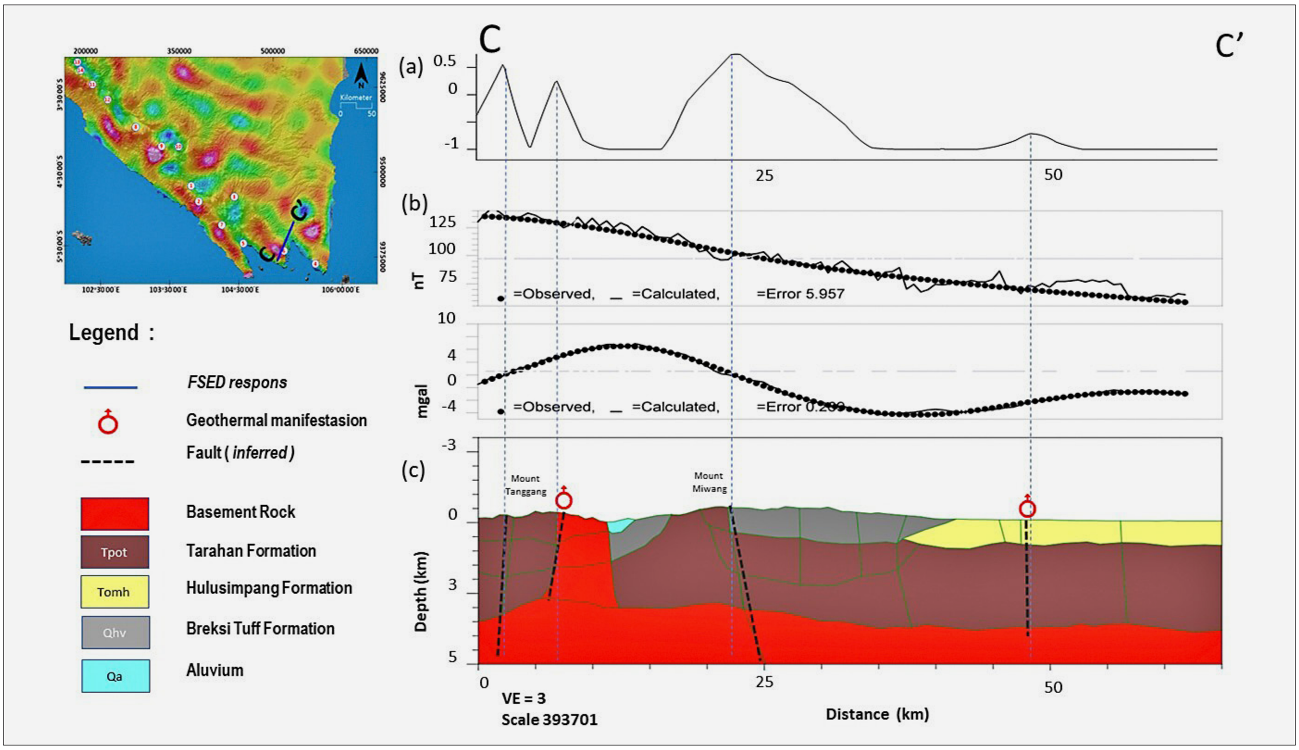

**Figure 14:** Cross-section C-C' of gravity and magnetic data modelling (a) FSED response delineating the geological structure, (b) residual gravity and magnetic response and (c) 2.5D gravity model of the geothermal prospect area.

the foundation layer, has a rock susceptibility value of 0.0007 sus and a density of 2.4–2.6 gr/cm$^3$.

**Figure 13** shows some of the results of modelling gravity and magnetic data collected in the area in conjunction with geothermal and structural geology studies. **Figure 13a** shows the location of the B-B' cross section profile in the area, with geothermal markers (red circles) and FSED responses (black thick lines). The map displays various geological formations, such as bedrock, the Kikim Formation, the Upper Simpang Formation, the Volcanic Andesit-Basalt Formation, and the Ranau Formation, in different colours. The 2.5D forward modelling results (see **Figure 13b, c**) indicate that the heat source is located at a depth of 4 km. Several rock formations are identified, namely the Kikim Formation (Tpok), with a density value of 2.3–2.6 gr/cm$^3$ and a rock susceptibility value of 0.0001–0.049 sus. The Hulu Simpang Formation (Tomh) has a density value of 2.5–2.6 gr/cm$^3$ and a rock susceptibility value of 0.0075–0.22 sus, located at depths varying from 1,500 m to 3,000 m. Young volcanic deposits derived from the Ranau Formation have a density value of 2.2–2.3 gr/cm$^3$ and a rock susceptibility value of -0.008–-0.0014 sus. The fault shown in the 2.5D model is also associated with the Kumering segment fault of the GSF. The segment's cutting of young volcanic rocks and the presence of geothermal manifestations serve as evidence. Furthermore, **Figure 14's** model reveals an intrusive body within the Gunung Kasih complex's rocks. To the west of this complex is a fault that originates from the West Semangko segment. This segment also controls the geothermal system located in the southern segment of Sumatra. The subsurface models made from the three models (see **Figures 12–14**) add to what is known about rock types. They also give us important information about the shape of the heat source and the rock features that determine how far it goes to the side. We can use this approach to pinpoint specific areas that necessitate more thorough geothermal exploration. Fault segments in the modelled GSF region indicate the presence of significant structural features that could play a role in geothermal fluid migration. As such, the resulting interpretation provides a clearer picture of the region's geothermal potential and the geologic factors that influence it.

Several significant components of the conceptual geothermal model in southern Sumatra are depicted in **Figure 15** to understand the development of the geothermal system in the region. The construction of the conceptual model depicted in **Figure 15** required an integration of diverse geophysical and geological datasets to accurately represent the geothermal system. Key inputs included magnetotelluric data from **Dyaksa et al. (2016)**, providing critical subsurface resistivity insight relevant to geothermal prospecting. Additionally, geological structures were delineated using FSED filtering techniques, which were subsequently interpreted and corroborated against established geological models. Curie Point Depth (CPD) calculations were utilized to generate heat flow contour maps, which were then validated with empirical drilling data published by **Hamdani et al. (2020)**. The conceptual model in **Figure 15** represents a novel synthesis of these data and has not been previously published. It specifically encompasses a cross-sectional profile along the A-A’ line, complemented by data from **Dyaksa et al. (2016)** to advance the understanding of the geothermal framework in southern Sumatra. The lithological references depicted in **Figure 1** provided foundational context for the model’s construction, ensuring alignment with known geological formations. The model depicts the intricate interplay among heat sources, reservoirs, claycaps, meteoric water, and faults, specifically those believed to form part of the GSF. The heat source is situated at a depth greater than 3 km. and shown in red, is the magma or hot rock that heats the water in the subsurface (see **Figure 13**). The heat source heats the hot water that collects in the reservoir, which is located below the ground surface and depicted in light blue. This reservoir matches the low gravity anomaly value. A claycap layer lies above the reservoir, preventing heat and fluid from escaping to the surface too quickly. This helps maintain reservoir pressure and temperature. The blue arrow indicates that meteoric water (rainwater) seeps into the ground and enters the geothermal system. Heat transfer from the underground heat source to the reservoir is illustrated by the red arrows. This heat warms the water in the reservoir, increasing the temperature and pressure. The hot water from the reservoir eventually reaches the surface through certain pathways, causing the manifestation of hot springs on the surface, as seen at Patah Hill, Besar Hill, Lumut Hill, and Balai Hill (see **Figure 15**).

The dashed line indicates a fault in the area, which is thought to be part of the GSF. These faults play an important role in circulating water and heat underground, facilitating the movement of hot water from reservoirs to the surface. Meteoric water descends through the fault, absorbing heat from underground sources to form a reservoir. High temperatures and pressures in the reservoir cause the water to rise to the surface as geothermal manifestations. Overall, this conceptual model reveals that the geothermal system in southern Sumatra relies heavily on fault structures, particularly the GSF, for heat and fluid transport. These faults not only provide pathways for meteoric water flow into the reservoir but also allow heat from underground magma sources to heat the water in the reservoir. By maintaining the reservoir's temperature and pressure, the claycap layer is essential to preserving the stability of the system.

The identification of the reservoir from magnetotelluric data by **Dyaksa et al. (2016)** revealed that the reservoir zone has higher resistivity values, located beneath the claycap layer with resistivity values of less than 10 ohms. The geologic structure that forms the geothermal system has a northwest - southeast direction, in line with the GSF. Geothermal manifestations such as hot springs and fumaroles are often found along this fault, indicating subsurface geothermal potential. We displayed the thermal gradient contours using CPD calculations of magnetic data correlated with temperature and pressure well logs. In the Rantau Dedap area, **Humaedi et al. (2016)** have conducted temperature and pressure measurements using well logs, while in Lumut Balai, **Hamdani et al. (2020)** also conducted similar measurements. The reser-

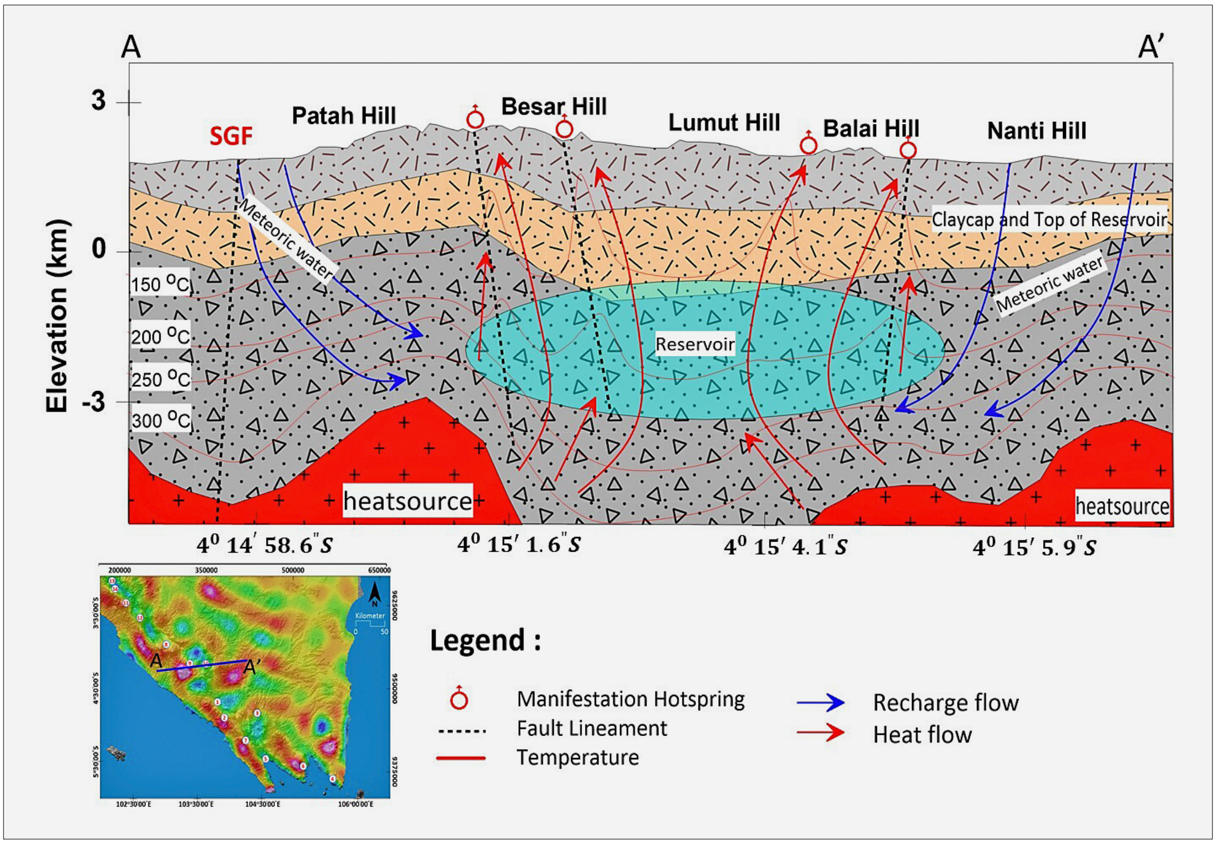

**Figure 15:** Conceptual model of geothermal in the southern Sumatra region

voir temperature is estimated to be between 200 to 280°C, helping to understand the geothermal potential and determine the best location for well drilling. This data also assists in assessing the efficiency and sustainability of geothermal potential, which supports Indonesia's sustainable development of renewable energy.

## 5. Conclusions

The geothermal potential of southern Sumatra is comprehensively evaluated in this study using gravity and magnetic data. This approach has proven effective in delineating geological structures such as faults, which are critical for geothermal exploration. According to the study, the western part of the study area's dominating high magnetic anomalies, which are coincident with residual gravity anomalies, indicate the presence of complex geological structures identified by FSED and are coincident with GSF segments in the southern part (Manna, Kumering, and Semangko segments). The identified structural trend is NW-SE trending. The gravity model revealed high subsurface anomalies, indicating magma intrusion, and low anomalies, indicating the presence of a reservoir. Other results identified intrusive volcanic rocks as heat sources, with thermal gradients ranging from 21.1°C/km - 31.6°C/km and heat flow between 55.1-79 mW/m². These high thermal gradients are mainly found beneath volcanic complexes such as the Bukit Barisan Mountains. The three resulting subsurface cross-section models show that structural features of the Sumatran Fault segments influence geothermal fluid migration. Modelling and interpretation of gravity data combined with analysis of magnetic data suggest a control mechanism by the GSF on geothermal systems in southern Sumatra.

### *Acknowledgement*

The authors would like to thank the Faculty of Mining and Petroleum Engineering, Institut Teknologi Bandung (ITB), for their administrative support.

## 6. References

Abdel Zaher, M., Saibi, H., Mansour, K., Khalil, A., abd Soliman, M. (2018): Geothermal exploration using airborne gravity and magnetic data at Siwa oasis, western desert, Egypt. Renewable and Sustainable Energy Reviews, 82, 3824-3832. https://doi.org/10.1016/j.rser.2017.10.088

Alif, S.M., Fattah, E.I., and Kholil, M. (2020): Geodetic slip rate and locking depth of east Semangko Fault derived from GPS measurement. Geodesy and Geodynamics, 11(3), 222-228. https://doi.org/10.1016/j.geog.2020.04.002

Aprina, P.U., Santoso, D., Alawiyah, S., Prasetyo, N., and Ibrahim, K. (2024): Delineating geological structure utilizing integration of remote sensing and gravity data: A study from Halmahera, north Molucca, Indonesia. Vietnam Journal of Earth Sciences. https://doi.org/10.15625/2615-9783/20010

Basantaray, A. K., and Mandal, A. (2022): Interpretation of gravity–magnetic anomalies to delineate subsurface configuration beneath east geothermal province along the Mahanadi rift basin: A case study of non-volcanic Hot Springs. Geothermal Energy, 10(1). https://doi.org/10.1186/s40517-022-00216-4

Bellier, O., dan Sébrier, M. (1994): Relationship between tectonism and volcanism along the great sumatran fault zone deduced by spot image analyses. Tectonophysics, 233 (3-4), 215-231. https://doi.org/10.1016/0040-1951(94)90242-9

Bellier, O., Bellon, H., Sébrier, M., Sutanto, and Maury, R. C. (1999): K-Ar age of the Ranau Tuffs: Implications for the Ranau caldera emplacement and slip partitioning in Sumatra (Indonesia). Tectonophysics, 312(2-4): 347–359. doi: 10.1016/ S0040-1951(99)00198-5

Bhattacharyya, B. K., and Leu, L. (1975): Analysis of magnetic anomalies over Yellowstone National Park: Mapping of Curie point isothermal surface for geothermal reconnaissance. Journal of Geophysical Research, 80(32), 4461-4465. https://doi.org/10.1029/jb080i032p04461

Bhattacharyya, B. K., and Leu, L. (1977): Spectral analysis of gravity and magnetic anomalies due to rectangular prismatic bodies. Geophysics, 42(1), 41-50. https://doi.org/10.1190/1.1440712

Burton, P.W., and Hall, T.R. (2014): Segmentation of the Sumatran fault. Geophysical Research Letters. 41(12). https://doi.org/10.1002/2014GL060242

Cooper, G.R.J., and Cowan, D.R. (2005): Differential reduction to the pole. School of Geosciences, University of the Witwatersrand, Johannesburg, South Africa and Cowan Geodata Services, 12 Edna Road, Dalkeith, Western Australia.

Curray, J.R. (2005): Tectonics and History of The Andaman Sea Region, Journal of Asian Earth Sciences, 25(1), 187–232, https://doi.org/10.1016/J.Jseaes.2004.09.001

Dyaksa, D. A., Ramadhan, I. I., and Ganefianto, N. (2016): Magnetotelluric Reliability for Exploration Drilling Stage: Study Cases in Muara Laboh and Rantau Dedap Geothermal Project, Sumatra, Indonesia. Proceedings, 41st Workshop on Geothermal Reservoir Engineering Stanford University, Stanford, California, SGP-TR-209.

Gaber, G. M., Saleh, S., and Kotb, A. (2024): 3D gravity and magnetic inversion modelling for geothermal assessment and temperature modelling in the central eastern desert and Red Sea, Egypt. Scientific Reports, 14(1). https://doi.org/10.1038/s41598-024-65131-z

Finlay, C.C., Maus, S., Bondar, T., Chambodut, A., Chernova, T.A, Chulliat, A., Golovkov, V.P, Hamilton, B., Hamoudi, M., Hulot, G., Langlais, B., Lesur, V., Lowes, F.J., Lühr, H., Kuang, W., Macmillan, S., McLean, S., Mandea, M., Manoj, C., Menvielle, M., Michelis, I., Olsen, N., Rauberg, J., Rother, M., Sabaka, T.J., Thebault, E., Thomson, A.W.P., Toffner-Clausen, L., Wardinski, I., and Zvereva, T.I. (2010): The 11th-generation international geomagnetic reference field. Geophysical Journal International, 183(3), https://doi.org/10.1111/j.1365-246X.2010.04804.x

Hamdani, M. R., Pratama, H. B., and Sutopo. (2020): Updating the conceptual model of Lumut Balai geothermal Field, south Sumatera, Indonesia using numerical simulation. IOP Conference Series: Earth and Environmental Science, 417(1), 012023. https://doi.org/10.1088/1755-1315/417/1/012023

Hamilton, W. (1979): Tectonic of Indonesian Region. US Government Printing. Washington

Hilemichaeil, S., Haile, T., and Yirgu, G. (2024): Integrated geophysical methods to constrain subsurface structures of Tulu Moye-Bora-Berecha axial volcanic complex, main Ethiopia rift: Implications for geothermal resources. Heliyon, 10(7), e28499. https://doi.org/10.1016/j.heliyon.2024.e28499

Hirt, C., Claessens, S., Fecher, T., Kuhn, M., Pail, R., and Rexer, M. (2013): New ultrahigh-resolution picture of earth's gravity field. Geophysical Research Letters, 40(16), 4279-4283. https://doi.org/10.1002/grl.50838

Hirt, C., Kuhn, M., Claessens, S., Pail, R., Seitz, K., and Gruber, T. (2014): Study of the Earth′s short-scale gravity field using the ERTM2160 gravity model. Computers & Geosciences, 73, 71-80. https://doi.org/10.1016/j.cageo.2014.09.001

Hirt, C., Yang, M., Kuhn, M., Bucha, B., Kurzmann, A., and Pail, R. (2019): SRTM2gravity: An ultrahigh resolution global model of gravimetric terrain corrections. Geophysical Research Letters, 46(9), 4618-4627. https://doi.org/10.1029/2019gl082521

Humaedi, M.T., Alfiady, Putra, A. P., Martikno, R., and Situmorang, J. (2016): A comprehensive well testing implementation during exploration phase in Rantau Dedap, Indonesia. IOP Conference Series: Earth and Environmental Science, 42, 012010. https://doi.org/10.1088/1755-1315/42/1/012010

Kongpet, P., and Kanjanapayont, P. (2024): Curie point depth from airborne magnetic data analysis for geothermal exploration in southern Thailand. Journal of Asian Earth Sciences, 261, 105984. https://doi.org/10.1016/j.jseaes.2023.105984

Liu, Y., Suardi, I., Huang, X., Liu, S., and Tong, P. (2021): Seismic velocity and anisotropy tomography of southern Sumatra. Physics of the Earth and Planetary Interiors, 316, 106722. https://doi.org/10.1016/j.pepi.2021.106722

McCaffrey, R., Zwick, P. C., Bock, Y., Prawirodirdjo, L., Genrich, J.F., Stevens, C.W., Puntodewo, S.S., and Subarya, C. (2000): Strain partitioning during oblique plate convergence in northern Sumatra: Geodetic and seismologic constraints and numerical modeling. Journal of Geophysical Research: Solid Earth, 105(B12), 28363-28376. https://doi.org/10.1029/1999jb900362

McCarthy, A.J., and Elders, C. F. (1997): Cenozoic deformation in Sumatra: Oblique subduction and the development of the sumatran fault system. Geological Society, London, Special Publications, 126(1), 355-363. https://doi.org/10.1144/gsl.sp.1997.126.01.21

Moghaddam, M.M., Mirzaei, S., Nouraliee, J., and Porkhial, S. (2016): Integrated magnetic and gravity surveys for geothermal exploration in central Iran. Arabian Journal of

Geosciences, 9(7). https://doi.org/10.1007/s12517-016-2539-y

Natawidjaja, D.H., Bradley, K., Daryono, M.R., Aribowo, S., and Herrin, J. (2017): Late Quaternary eruption of the Ranau caldera and new geological slip rates of the sumatran fault zone in southern Sumatra, Indonesia. Geoscience Letters, 4(1). https://doi.org/10.1186/s40562-017-0087-2

Núñez Demarco, P., Prezzi, C., and Sánchez Bettucci, L. (2021): Review of Curie point depth determination through different spectral methods applied to magnetic data. Geophysical Journal International, 224(1), 17-39. https://doi.org/10.1093/gji/ggaa361

Nurseto, S. T., Julia Satriani, R. A., Thamrin, M. H., and Suryantini, N. (2021): Productive structural geology in Volcanogenic system: A case study of Lumut Balai geothermal Field, Indonesia. IOP Conference Series: Earth and Environmental Science, 732(1), 012013. https://doi.org/10.1088/1755-1315/732/1/012013

Oksum, E., Le, D.V., Vu, M.D., Nguyen, T.H.T., and Pham, L.T. (2021): A novel approach based on the fast sigmoid function for interpretation of potential field data. Bulletin of Geophysics and Oceanography. 62 (3), 543–556.

Okubo, Y., Matsushima, M., Matsubayashi, O., and Utsugi, M. (1985): Magnetization intensity and Curie point depth in northeast Japan. Tectonophysics, 114 (1–4), 365–376.

Pham, L. T., Ghomsi, F. E., Vu, T. V., Oksum, E., Steffen, R., and Tenzer, R. (2023): Mapping the structural configuration of the western Gulf of Guinea using advanced gravity interpretation methods. Physics and Chemistry of the Earth, Parts A/B/C, 129, 103341. https://doi.org/10.1016/j.pce.2022.103341

Pham, L. T., and Prasad, K. N. (2024): Gravity patterns and crustal architecture of the south-central Indian ridge at 22°-17°S: Evidence for the asymmetric ridge accretion. Journal of Asian Earth Sciences, 260, 105966. https://doi.org/10.1016/j.jseaes.2023.105966

Prawirodirdjo, L., Bock, Y., Genrich, J. F., Puntodewo, S. S., Rais, J., Subarya, C., and Sutisna, S. (2000): One century of tectonic deformation along the sumatran fault from triangulation and Global Positioning System surveys. Journal of Geophysical Research: Solid Earth, 105(B12), 28343-28361. https://doi.org/10.1029/2000jb900150

Pusat Sumber Daya Geologi. (2004): Data Geologi, Geokimia dan Geofisika Danau Ranau. Pusat Sumber Daya Geologi (PSDG), Bandung.

Rao, V. B., and Satyanarayana Murty, B. V. (1973): Note on Parasnis' method for surface rock densities. Pure and applied geophysics, 110(1), 1927-1931. https://doi.org/10.1007/bf00876555

Reynolds, J.M. (1997): An Introduction to Applied and Environmental Geophysics. John Wiley & Sons. Chichester.

Robinson, E. S., and Coruh, C. (1988): Basic exploration geophysics. John Wiley & Sons.

Saada, S.A. (2016): Curie point depth and heat flow from spectral analysis of aeromagnetic data over the northern part of western desert, Egypt. Journal of Applied Geophysics, 134, 100-111. https://doi.org/10.1016/j.jappgeo.2016.09.003

Safani, J., Ibrahim, K., Deni, W., Rubaiyn, A., Firdaus, F., and Harisma, H. (2023): Interpreting structural configuration of the Sengkang basin of Indonesia using edge detection and 3-D Euler deconvolution to satellite gravity data. Turkish Journal of Earth Sciences, 32(7), 894-914. https://doi.org/10.55730/1300-0985.1881

Sieh, K. dan Natawidjaja, D. (2000): Neotectonics of the Sumatran Fault, Indonesia, Journal of Geophysical Research, 105 (B12), 28.295–28.326.

Siringoringo, L.P., Sapiie, B., Rudyawan, A., and Sucipta, I.G. (2024): Origin of high heat flow in the back-arc basins of Sumatra: An opportunity for geothermal energy development. Energy Geoscience, 5(3), 100289. https://doi.org/10.1016/j.engeos.2024.100289

Spector, A., and Grant, F.S. (1970): Statistical models for interpreting aeromagnetic data. Geophysics, 35(2), 293-302. https://doi.org/10.1190/1.1440092

Sukmono, S., Zen, M., Kadir, W., Hendrajaya, L., Santoso, D., and Dubois, J. (1996): Fractal geometry of the Sumatra active fault system and its geodynamical implications. Journal of Geodynamics, 22(1-2), 1-9. https://doi.org/10.1016/0264-3707(96)00015-4

Tanaka, A., Okubo, Y., and Matsubayashi, O. (1999): Curie point depth based on spectrum analysis of the magnetic anomaly data in east and Southeast Asia. Tectonophysics, 306(3-4), 461-470. https://doi.org/10.1016/s0040-1951(99)00072-4

Veloso, E.E., Gomila, R., Cembrano, J., González, R., Jensen, E., and Arancibia, G. (2015): Stress fields recorded on large-scale strike-slip fault systems: Effects on the tectonic evolution of crustal slivers during oblique subduction. Tectonophysics, 664, 244-255.

Widiyantoro, S., Supendi, P., Rawlinson, N., Daryono, M.R., and Rosalia, S. (2024): A note on the seismicity of Sumatra, western Sunda arc, Indonesia, in relation to the potential for back-arc thrusting. Scientific Reports, 14(1). https://doi.org/10.1038/s41598-024-64076-7

Zaher, M.A., Saibi, H., Mansour, K., Khalil, A., and Soliman, M. (2018): Geothermal exploration using airborne gravity and magnetic data at Siwa oasis, western desert, Egypt. Renewable and Sustainable Energy Reviews, 82, 3824-3832. https://doi.org/10.1016/j.rser.2017.10.088

Zhang, J., Hao, T., Dong, M., Xu, Y., Wang, B., Ai, Y., and Fang, G. (2020): Investigation of geothermal structure of the Sulawesi, using gravity and magnetic method. Science China Earth Sciences, 64(2), 278-293. https://doi.org/10.1007/s11430-020-9659-3

## SAŽETAK

### Nove spoznaje o strukturnome modelu južne Sumatre u Indoneziji dobivene korištenjem gravimetrijskih i magnetometrijskih podataka: implikacije za geotermalne resurse

Otok Sumatra nastao je složenim tektonskim procesima koji su rezultirali nizom geoloških resursa, uključujući i geotermalni potencijal. Rasjedi, posebice Veliki sumatranski rasjed (GSF), povezani su s geotermalnim pojavama na površini. Cilj ovoga istraživanja bio je napraviti temeljitu procjenu geotermalnoga potencijala u južnoj Sumatri korištenjem kombinacije magnetnih i gravimetrijskih podataka. Rezultati upućuju na to da su izvor topline na Sumatri intruzivne vulkanske stijene gustoće 2,8 g/cm³ i vrijednosti susceptibiliteta od 0,007, koje se rasprostiru od zapada prema jugu u smjeru sjeverozapad-jugoistok. Ove stijene dio su formacije Kikim (Tpok) nastale iz ostataka magme planine Bukit Besar, Bukit Lumut i Bukit Balai, na dubini većoj od 7 km. Rezervoarska zona u središtu tijela vjerojatno je uzrokovana pukotinskom zonom rasjeda Sumatra ili sedimentnim stijenama koje se sastoje od formacija Hulusimpang i Gumai gustoće 2,6 g/cm³ i vrijednosti susceptibiliteta od 0,075 na dubini od 1000 do 1500 m. Toplinski tok kreće se od 55,1 do 79 mW/m², a geotermalni gradijent kreće se u rasponu između 21,1 i 31,6 °C/km. Drugo je otkriće veliki geotermalni gradijent opažen ispod vulkanskih kompleksa uključujući područje planina Bukit Barisan. Rasjedna zona s pružanjem sjeverozapad-jugoistok i paralelna s GSF-om upućuje na to da ovaj rasjed kontrolira geotermalni sustav na Sumatri, pružajući nove uvide u mehanizam kontrole geotermalnoga sustava. Integracija gravimetrijskih i magnetometrijskih podataka upućuje na nove odnose između tektonskih struktura u GSF zoni i do sada neistraženoga geotermalnog potencijala.

**Ključne riječi:**
gravimetrija, magnetometrija, geotermalni, Veliki sumatranski rasjed

## Author's contribution

**Irfan Prasetyo (1)** (M.Eng., geophysical engineer with expertise in applied geophysics, especially in geothermal exploration) performed the gravity and magnetic data collection, provided magnetic data processing and interpretation, original drafting, edited the draft, and managed project administration. **Wawan Gunawan Abdul Kadir (2)** (PhD, Professor of Gravity and Magnetics) interpreted the gravity and magnetic data, edited drafts, served as the first supervisor, and managed project administration. **Dadi Abdurrahman (3)** (PhD, geophysical engineer with expertise in applied geophysics, especially in the gravity method) interpreted the gravity and magnetic data, served as the second supervisor, and edited drafts. **Darharta Dahrin (4)** (PhD, Associate Professor, expert in gravity and magnetic methods) interpreted the gravity and magnetic data, served as the third supervisor, and edited drafts. **Khalil Ibrahim (5)** (M.Eng., geophysical engineer with expertise in geophysical exploration) prepared the manuscript, interpreted data, and edited drafts. **Andri Kurniawan (6)** (M.Eng., geophysical engineer with expertise in seismology) interpreted data and edited drafts. All authors read and approved the final manuscript.